Hydrogenic donor impurity states and intersubband optical absorption spectra of monolayer transition metal dichalcogenides in dielectric environments

Shu-Dong Wu(吴曙东)†

College of Physics Science and Technology, Yangzhou University, Yangzhou 225002, *China*

(Received 5 June 2022; revised manuscript received 8 October 2022; accepted manuscript online 19 October 2022)

The hydrogenic donor impurity states and intersubband optical absorption spectra in monolayer transition metal dichalcogenides (ML TMDs) under dielectric environments are theoretically investigated based on a two-dimensional (2D) nonorthogonal associated Laguerre basis set. The 2D quantum confinement effect together with the strongly reduced dielectric screening results in the strong attractive Coulomb potential between electron and donor ion, with exceptionally large impurity binding energy and huge intersubband oscillator strength. These lead to the strong interaction of the electron with light in a 2D regime. The intersubband optical absorption spectra exhibit strong absorption lines of the non-hydrogenic Rydberg series in the mid-infrared range of light. The strength of the Coulomb potential can be controlled by changing the dielectric environment. The electron affinity difference leads to charge transfer between ML TMD and the dielectric environment, generating the polarization-electric field in ML TMD accompanied by weakening the Coulomb interaction strength. The larger the dielectric constant of the dielectric environment, the more the charge transfer is, accompanied by the larger polarization-electric field and the stronger dielectric screening. The dielectric environment is shown to provide an efficient tool to tune the wavelength and output of the mid-infrared intersubband devices based on ML TMDs.

Keywords: monolayer transition metal dichalcogenides, hydrogenic donor impurity, intersubband optical absorption, dielectric environment, nonorthogonal associated Laguerre basis

PACS: 73.30.+y, 71.55.–I, 71.35.Cc, 77.22.Ch **DOI:** 10.1088/1674-1056/ac9b30

1. Introduction

During the past few years, monolayer transition metal dichalcogenides (ML TMDs) such as MoS_2, $MoSe_2$, $MoTe_2$, WS_2, and WSe_2 have attracted a great deal of attention among researchers due to their promising potential applications in next-generation two-dimensional (2D) electronic and optoelectronic devices.[1–9] Owing to their 2D structure of three-atom thickness, the electronic and optical properties of ML TMDs show extraordinary behaviors. For instances, in contrast to their bulk counterparts, these ML TMDs exhibit direct-gap properties in a visible to near-infrared light range located at the two inequivalent K and K' valleys of the Brillouin zone.[10,11] Moreover, the broken inversion symmetry and strong spin–orbit coupling couple the electronic spin and the valley pseudospin, leading to the spin–valley locking effect: σ^+ light induces transitions at the K valley, while σ^- light induces transitions at the K' valley.[12–15]

Since Bastard's[16] pioneer work on the study of the binding energy of a hydrogenic impurity within an infinite potential-well structure, a lot of theoretical researches have been devoted to the study of the impurity-related intersubband transitions in various confining systems.[17–25] Since the hydrogenic donor atom has one more valence electron than host atom, it is analogous to a hydrogen atom when the donor atom is incorporated at substitutional site of the host lattice. It is essential to know the electronic structure of impurity atoms in semiconductors for understanding the physics of optoelectronic devices.[26] Since the electron motion is restricted to a plane in an ML TMD, quantum confinement effect is more apparent than in the bulk counterpart. At the same time, the three-atom thickness greatly reduces the dielectric screening. These properties significantly enhance the Coulomb interaction between the electron and the donor ion, and the electron is expected to be more tightly bound by the donor ion.[27–31] In the atomically thin limit, the Coulomb interaction is notably sensitive to the surrounding dielectric environments, *i.e.*, the substrate and the cap layer.[32,33] Placing ML TMDs under different dielectric environments can modulate the Coulomb interaction strength. The impurity states in ML TMDs have been accurately evaluated by using first-principles electronic structure calculations based on density functional theory, which includes complicated and expensive calculations of the atomistic supercells with large size.[34–36] The effective-mass approximation (EMA) of Kohn and Luttinger[37,38] can overcome these shortcomings, which has been highly successful in describing the electronic structure of shallow-level impurities in semiconductors. Since the EMA does not include complicated calculations of the atomistic structure,[39] we employ it to focus on the understanding of the effect of an impurity on the electronic structures of the ML TMDs.

†Corresponding author. E-mail: sdwu@yzu.edu.cn

© 2023 Chinese Physical Society and IOP Publishing Ltd

The presence of impurities has an important influence on the optical response of ML TMDs. If the energy corresponding to the frequency of the external light is smaller than the bandgap energy, the intersubband optical transitions may occur between impurity states by absorbing a photon.[40] The impurity-related intersubband transitions in a 2D structure as a mid-infrared active medium are attractive due to huge optical cross sections, long lifetimes of impurity states, and sensitivity to normal incident radiation.[41,42] Therefore, the investigation of impurity-related optical properties in ML TMDs is of particular importance in designing and developing devices such as photodetectors for mid-infrared region. As far as we know, there have not been theoretical investigations on hydrogenic donor impurity states and impurity-related optical spectra in ML TMDs under different dielectric environments. This has motivated us to investigate the yet unexplored domain of impurity-related optical properties in ML TMDs. In this paper, we employ a variationally optimized diagonalization method based on a 2D nonorthogonal associated Laguerre basis set and investigate systematically the hydrogenic donor impurity states and their intersubband absorption spectra in ML TMDs under different dielectric environments within the EMA. We also make a comparison of main features among five TMDs, such as the impurity binding energy, Bohr radius, and intersubband oscillator strength.

The remainder of this paper is organized as follows. In Section 2, we present a theoretical model and numerical procedure. In Section 3, the numerical results for the impurity electron energy, wave functions and intersubband absorption spectra are presented and discussed. Finally, some conclusions are drawn from the present study in Section 4. A fully analytical expression for the matrix elements of the screened Coulomb potential is further derived in Appendix A.

2. Computational details

Consider a hydrogenic donor impurity located in the center of ML TMDs which is surrounded by dielectric environments. Within the effective-mass approximation, the 2D Hamiltonian of a hydrogenic donor impurity in ML TMDs under the dielectric environments is written in polar coordinates (r,φ) as

$$H=-\frac{\hbar^2}{2m_{\rm e}^*}\left(\frac{\partial^2}{\partial r^2}+\frac{1}{r}\frac{\partial}{\partial r}+\frac{1}{r^2}\frac{\partial^2}{\partial\varphi^2}\right)+V(r,\varphi), \tag{1}$$

where $m_{\rm e}^*$ is the effective mass of the electron and r is the in-plane distance between the electron and the donor ion.

The screened Coulomb potential $V(r,\varphi)$ describes the attractive interaction of the electron with the related donor ion, which is derived by Keldysh and given below:[43–45]

$$V(r,\varphi)=-\frac{e^2}{4\pi\kappa\varepsilon_0}\cdot\frac{\pi}{2r_0}\left[{\rm H}_0\left(\frac{r}{r_0}\right)-{\rm Y}_0\left(\frac{r}{r_0}\right)\right], \tag{2}$$

where e is the absolute value of the electron charge; ε_0 is the permittivity in vacuum; ${\rm H}_0(x)$ and ${\rm Y}_0(x)$ are the zero-order Struve function and the Bessel function of the second kind, respectively; $r_0=2\pi\chi_{\rm 2D}/\kappa$ is the dielectric screening length directly related to the 2D polarizability $\chi_{\rm 2D}$ of the ML TMDs with dielectric environments; κ is the mean relative dielectric constant of the surrounding matrix. Here we consider the ML TMD sandwiched between a substrate with dielectric constant $\varepsilon_{\rm sub}$ and vacuum on the other side, in which case $\kappa=(1+\varepsilon_{\rm sub})/2$.

The 2D Schrödinger equation is given by

$$H\psi=E\psi, \tag{3}$$

where E and ψ are the eigenvalue and the eigenstate of the impurity electron, respectively.

Owing to the screened Coulomb potential, an exact analytical solution to the Schrödinger equation (3) is not possible. To obtain an accurate numerical solution, it is important to use a sufficiently flexible basis set to describe the nodes and turning points of the wave function, and the donor electron wave function is expanded in terms of a set of 2D nonorthogonal associated Laguerre basis functions in polar coordinates (r,φ) as shown below:[46,47]

$$\psi(r,\varphi)=\sum_{n=0}^{n_{\max}}\sum_{l=-l_{\max}}^{l_{\max}}C_{nl}\Phi_{nl}(r,\varphi), \tag{4}$$

where

$$\Phi_{nl}(r,\varphi)=R_{nl}(r)\cdot\frac{1}{\sqrt{2\pi}}{\rm e}^{{\rm i}l\varphi}, \tag{5a}$$

with

$$R_{nl}(r)=\left[\frac{n!}{(n+2|l|)!(2n+2|l|+1)}\right]^{1/2}\zeta(\zeta r)^{|l|}\times\exp\left(-\frac{\zeta r}{2}\right){\rm L}_n^{2|l|}(\zeta r). \tag{5b}$$

where C_{nl} are the expansion coefficients; $n=0,1,2,\ldots$, and $l=0,\pm1,\pm2,\ldots$, are the radial and angular momentum quantum numbers, respectively; $\Phi_{nl}(r,\varphi)$ is a complete set of 2D normalized nonorthogonal associated Laguerre basis functions for each n and l in the domain $0\le r<\infty$ and $0\le\varphi\le2\pi$; and $R_{nl}(r)$ is a normalized radial basis function; ${\rm L}_n^{2|l|}(\zeta r)$ is an associated Laguerre polynomial; $(\zeta r)^{|l|}$ describes the radial behavior of the wave function near the origin; the exponential term $\exp(-\zeta r/2)$ describes the decay of the radial part of the wave function far from the origin, which is determined by an adjustable variational parameter ζ. Owing to computational limitation, the infinite summations over n and l have to be truncated at the maximum radial quantum number $(n_{\max})$ and the maximum angular momentum quantum number $(l_{\max})$ chosen in an actual run, respectively. For simplicity, $n_{\max}=l_{\max}=N=10$ is assumed to be the basis size in this

calculation, which ensures that the eigenvalues is insensitive to the further increase in N.[46,47]

Multiplying the left-hand side of Eq. (3) by a conjugate function in our basis set and integrating over the coordinates, the resulting generalized eigenvalue equation yields the following equation:

$$HC = ESC, \tag{6}$$

where the matrix elements of the Hamiltonian H are given by

$$\begin{aligned} \mathrm{H}_{n'l',nl} &= \frac{\hbar^2}{2m_{\mathrm{e}}^*}\delta_{l',l}\Bigg\{\frac{\zeta^2}{4}\delta_{n',n} \\ &+\frac{\zeta^2}{4}\left[\frac{n(n+2|l|)}{(2n+2|l|-1)(2n+2|l|+1)}\right]^{1/2}\delta_{n',n-1} \\ &+\frac{\zeta^2}{4}\left[\frac{(n+1)(n+2|l|+1)}{(2n+2|l|+1)(2n+2|l|+3)}\right]^{1/2}\delta_{n'-1,n}\Bigg\} \\ &+V_{n'l',nl}, \end{aligned} \tag{7a}$$

and the matrix elements of the overlap integral S are given by

$$\begin{aligned} S_{n'l',nl} &= \delta_{n',n}\delta_{l',l} \\ &-\left[\frac{n(n+2|l|)}{(2n+2|l|-1)(2n+2|l|+1)}\right]^{1/2}\delta_{n',n-1}\delta_{l',l} \\ &-\left[\frac{(n+1)(n+2|l|+1)}{(2n+2|l|+1)(2n+2|l|+3)}\right]^{1/2}\delta_{n'-1,n}\delta_{l',l}, \end{aligned} \tag{7b}$$

where $\delta_{n',n}$ and $\delta_{l',l}$ are the Kronecker delta functions, and $V_{n'l',nl}$ are the matrix elements of the screened Coulomb potential $V(r,\varphi)$. The associated Laguerre functions are flexible, allowing the analytical evaluations of the most expensive integrals, thus decreasing the computational cost of the simulations. In order not to get involved in explicit integrals in the matrix elements of the screened Coulomb potential, the analytical expression of $V_{n'l',nl}$ in Eq. (7a) is derived in detail in Appendix A. This analytical expression greatly simplifies the calculation because most of the computational time is spent on the diagonalization of the matrix rather than on the calculation of the integrals. It can be seen that both the Hamiltonian matrix and the overlap matrix are sparse matrices. The associated Laguerre basis functions are local polynomial functions with continuous first and second derivatives. Moreover, the nonorthogonal associated Laguerre basis set is nonorthogonal basis set which contains both bound discrete states and unbound continuous states. These are the advantages of nonorthogonal associated Laguerre representation. Therefore, the 2D nonorthogonal associated Laguerre basis set converges faster than other basis sets.[46,47]

After calculating H and S, the variationally optimized diagonalization method is used to obtain the generalized eigenvalues and eigenstates numerically. By varying the value of ζ from state to state, the minimum of the energy is obtained within the selected size of the basis set. The ordinary procedure is as follows. First, initializing ζ for each energy level E_{nl}, then diagonalizing the generalized eigenvalue equation (6) to obtain E_{nl} and the wave function $\psi_{nl}(r,\varphi)$. Finally, adjusting ζ until the minimum of E_{nl} is found. In this way, both E_{nl} and $\psi_{nl}(r,\varphi)$ of impurity states can be determined. Therefore it can be carried out on a personal computer.

In order to calculate the absorption coefficient, we consider the interaction between the linear polarized light of angular frequency ω and ML TMDs. Owing to the azimuthal symmetry of the screened Coulomb potential, the intersubband optical absorption is independent of the photon polarization. Hence, we choose the light polarized along the x direction as incident light that only excites electrons in the K/K' valley of the Brillouin zone. Based on Fermi's golden rule, the intersubband optical absorption spectra are given by[48]

$$\alpha(\hbar\omega) \propto \sum_f O_{if}\delta(E_{fi}-\hbar\omega), \tag{8}$$

where $\hbar\omega$ is the incident photon energy. Assuming that there exists a Fermi–Dirac distribution in the low temperature limit, only transition from occupied initial state $|i\rangle$ to unoccupied final state $|f\rangle$ is considered in the summation. The $E_{fi}=E_f-E_i$ is the energy difference between the final state $|f\rangle$ of energy E_f and the initial state $|i\rangle$ of energy E_i.

Taking into account the impurity level degeneracy and valley degeneracy, the intersubband oscillator strength between initial state $|i\rangle$ and final states $|f\rangle$ is defined as[48]

$$O_{if} = g_l g_v \times \frac{2m_{\mathrm{e}}^* E_{fi}}{\hbar^2}\left|M_{fi}\right|^2, \tag{9}$$

where $g_l = 2$ is the impurity level degeneracy and $g_v = 2$ is the valley degeneracy.

The transition matrix element M_{fi} between the final state $|f\rangle$ and the initial state $|i\rangle$ is defined as

$$\begin{aligned} M_{fi} &= \langle f|x|i\rangle = \langle f|r\cos\varphi|i\rangle \\ &= \frac{1}{2}\langle f|r(\mathrm{e}^{\mathrm{j}\varphi}+\mathrm{e}^{-\mathrm{j}\varphi})|i\rangle \\ &= \frac{1}{2}(\delta_{l_f,l_i-1}+\delta_{l_f,l_i+1})\int_0^\infty \psi_f^*(r)\psi_i(r)r^2\,\mathrm{d}r. \end{aligned} \tag{10}$$

In the standard atomic notations nQ of the three-dimensional (3D) hydrogen atom, where $Q = s,p,d,\ldots$ corresponds to the angular momentum quantum number $l = 0,1,2,\ldots$ which mark the states of hydrogen atom. If the standard notations is still used in two dimensions, then $l=0$ defines the s-like states ($1s$, $2s$, $3s$, …), $l=\pm1$ defines the p-like states ($2p_{\pm1}$, $3p_{\pm1}$, $4p_{\pm1}$, …), and $l=\pm2$ defines the d-like states ($3d_{\pm2}$, $4d_{\pm2}$, $5d_{\pm2}$, …). As the screened Coulomb potential has azimuthal symmetry, the impurity states with the same n and $|l|$ are degenerate. For simplicity, the subscripts ($\pm1,\pm2,\ldots$) are usually omitted, that is, the $1s$, $2s$, $2p$, $3s$, $3p$, $3d$, *etc.* are used henceforth. One can see from Eq. (10) that

the selection rules for intersubband transitions between the impurity states coincide with the selection rule, *i.e.*, $\Delta l = l_f - l_i = \pm 1$. Since the initial state is $1s$ state, the final states correspond to p-like states. Considering the dipole selection rules, the allowed transitions are $1s \to 2p_{-1}$, $1s \to 2p_{+1}$, $1s \to 3p_{-1}$, $1s \to 3p_{+1}$, $1s \to 4p_{-1}$, $1s \to 4p_{+1}$, *etc*. For instance, the intersubband oscillator strength of $1s \to 2p$ transition is twice that of $1s \to 2p_{-1}$ or $1s \to 2p_{+1}$ transition.

The Dirac delta function in Eq. (8) is replaced by Lorenz function of finite width, *i.e.*

$$\delta(E_{fi} - \hbar\omega) = \frac{\Gamma}{\pi[(E_{fi} - \hbar\omega)^2 + \Gamma^2]}, \tag{11}$$

where Γ is the hydrogenic impurity linewidth and taken as $\Gamma = 5$ meV for all the bound state transitions.

3. Results and discussion

3.1. Impurity states

To study the impurity states in ML TMDs, we focus on five widely used semiconductors-MoS_2, $MoSe_2$, $MoTe_2$, WS_2, and WSe_2 whose material parameters used in the present paper are the same as those in Ref. [46].

To provide an insight into how strongly the electron is bound by the donor ion, we can make use of the average distance of $1s$ state between the electron and donor ion as Bohr radius $r_{1s} = \sqrt{\langle \psi_{1s}(r)| r^2 |\psi_{1s}(r)\rangle}$. The impurity binding energy E_b, Bohr radius r_{1s}, intersubband oscillator strength O_{if}, and intersubband transition energy E_{fi} for five ML TMDs with $\kappa = 1$ are listed in Table 1. In ML TMDs, with respect to their bulk counterparts, the three-atom thickness strongly reduces the dielectric screening, resulting in an exceptionally large E_b on the order of several hundreds of meV ($\sim$ 433 meV–613 meV), which are several orders of magnitude larger than the impurity binding energy in conventional bulk semiconductors. When the value of r_0 increases, $V(r, \varphi)$ becomes a shallower potential. The dielectric screening length weakens the electrostatic interaction between the electron and the related donor ion, and consequently the impurity binding energy decreases. Of the five TMDs, MoS_2 has the largest E_b, however $MoTe_2$ has the smallest E_b. Correspondingly, both localization and magnitude of the wave function increase, which means that the average distance between the electron and the donor ion decreases and that is immediately followed by the increase of the impurity binding energy. In accordance with Coulomb's law, the impurity binding energy E_b is inversely proportional to the average distance r_{1s} between the electron and the donor ion. Surprisingly, the r_{1s} (0.930 nm) of WS_2 is greater than that (0.793 nm) of $MoSe_2$. However, the E_b (605.655 meV) of WS_2 is greater than that (555.46 meV) of $MoSe_2$, which indicates that it breaks Coulomb's law. The corresponding r_{1s} is about 1 nm. Although it is not very large, it is still much larger than the lattice constant, demonstrating that the EMA is still suitable for calculating impurity states. Compared with their bulk counterparts, the 2D quantum confinement effect together with the strongly reduced dielectric screening results in a huge intersubband oscillator strength. This leads to the strong light-matter interaction in a 2D regime. The intersubband oscillator strength is almost the same for five TMDs. However, the intersubband transition energy is different. It is largest in WS_2 and smallest in $MoTe_2$.

Table 1. Values of impurity binding energy (E_b), Bohr radius (r_{1s}), intersubband oscillator strength (O_{if}), and intersubband transition energy E_{fi} of hydrogenic donor impurity in five ML TMDs with $\kappa = 1$, with energy and radius of impurity electron being in units meV and nm, respectively.

	MoS_2	$MoSe_2$	$MoTe_2$	WS_2	WSe_2
E_b	613.359	555.46	433.195	605.655	541.475
r_{1s}	0.795	0.793	0.908	0.930	0.973
O_{if} $(1s \to 2p)$	1.674	1.686	1.698	1.652	1.663
E_{fi} $(1s \to 2p)$	236.266	203.124	149.84	252.364	217.437
O_{if} $(1s \to 3p)$	0.153	0.152	0.150	0.156	0.155
E_{fi} $(1s \to 3p)$	375.5	326.294	243.167	393.757	342.341
O_{if} $(1s \to 4p)$	0.045	0.045	0.044	0.047	0.078
E_{fi} $(1s \to 4p)$	446.136	390.416	292.964	462.338	404.274

Figure 1 shows the energy level diagram of the hydrogenic donor impurity for six low-lying states in five ML TMDs with $\kappa = 1$. Here we limit our description to the six energetically low-lying impurity states, that is, the $1s$, $2s$, $2p$, $3s$, $3p$, and $3d$ states. The impurity energy values in five ML TMDs with $\kappa = 1$ are presented in Table 2. As a consequence of the attractive Coulomb potential between electron and donor ion, the energy levels are a set of discrete non-hydrogenic Rydberg states with negative energy values, which appear in an anomalous energy level ordering of the orbital angular momentum l as indicated below. $E_{1s} < E_{2p} < E_{2s} < E_{3d} < E_{3p} < E_{3s}$. As the screened Coulomb potential has azimuthal symmetry, but it is not an exact $-e^2/4\pi\kappa\varepsilon_0 r$ potential, the dielectric screening just removes the degeneracy of the impurity states with the same n but different $|l|$, resulting in the splitting of the degenerate levels and the renormalizing of the impurity energy spectra. For instance, the asymmetric confinement caused by the dielectric screening effect pulls down $2p$ energy states, which lays energetically below $2s$ state. They deviate significantly from a bare 2D hydrogen-like model where the states with the same n but different $|l|$ are degenerate. For a fixed value of n, the lowest energy is associated with the state of highest $|l|$, *i.e.*, the shell degeneracies in the states are partially removed. In the case of the ML MoS_2, the energy level ratio of the adjacent s-type states is $E_{1s} : E_{2s} : E_{3s} = 1 : 0.51 : 0.34$, which deviates significantly from a 2D bare hydrogen-like model of

$E_{1s} : E_{2s} : E_{3s} = 1 : 0.11 : 0.04$, showing a strong decrease of the adjacent level spacing as compared with the counterpart for the case of bare hydrogen-like Coulomb potential. This is because the screened Coulomb potential near the origin diverges faster in logarithmic form than the bare hydrogen-like Coulomb potential.

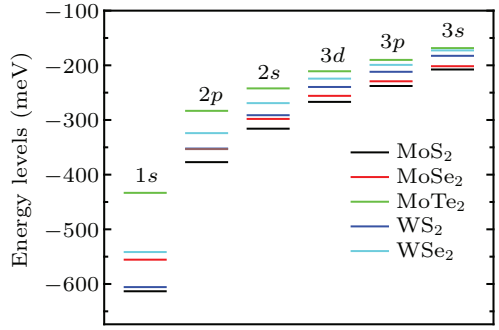


Fig. 1. Energy level diagram of the hydrogenic donor impurity for six low-lying states in five ML TMDs with $\kappa = 1$.

Table 2. Energy levels (in unit meV) of hydrogenic donor impurity for six low-lying states in five ML TMDs with $\kappa = 1$.

State	MoS_2	$MoSe_2$	$MoTe_2$	WS_2	WSe_2
1*s*	–613.359	–555.46	–433.195	–605.655	–541.475
2*p*	–377.094	–352.336	–283.355	–353.291	–324.038
2*s*	–315.853	–298.101	–242.225	–291.253	–269.165
3*d*	–266.942	–255.812	–210.878	–239.595	–224.398
3*p*	–237.859	–229.167	–190.028	–211.898	–199.134
3*s*	–207.582	–201.593	–168.556	–182.69	–172.671

In Fig. 2, the energy spectra of the hydrogenic donor impurity for six low-lying states as a function of κ for five ML TMDs are compared with each other. Several series of calculations with κ varying from 1 to 15 are performed. For example, ML TMDs are placed in a variety of dielectric environments, such as Si, SiO_2, hBN, HfO_2, and Al_2O_3, which have different macroscopic dielectric constants.[49] The attractive Coulomb interaction of the donor ion results in the discrete bound states of negative energy. For five TMDs, the variation trends of the energy spectra as a function of κ are similar and do not show any strong material dependence. With κ increasing, the energy levels increase monotonically and converge to the bulk situation. This is because there are different values of electron affinity between ML TMD and the surrounding dielectric environment. The electron affinity difference leads to charge transfer between ML TMD and the surrounding dielectric environment, which generates the polarization-electric field in ML TMD. This leads to the separation between the electron and the related donor ion. The larger the dielectric constant of the dielectric environment, the more the charge transfer is, accompanied by the larger polarization-electric field with the stronger dielectric screening. Therefore, the dielectric screening introduced by the dielectric environment weakens the Coulomb interaction strength, and consequently, the energy level increases. The 1*s* state increases at a higher rate than other states. This comes from the fact that the 1*s* state is more localized near donor ion and more influenced by κ. For a given κ, the relative ordering of the energy level is found to be as follows: $MoTe_2 < MoSe_2 < MoS_2 < WSe_2 < WS_2$. This is related to the dielectric screening length and effective mass of electron. At small r, $V(r,\varphi) \sim -e^2/4\pi\kappa\varepsilon_0 r_0 \log(r/2r_0)$, and at large r, $V(r,\varphi) \sim -e^2/4\pi\kappa\varepsilon_0 r$. Obviously, the energy spectra of impurity states strongly depend on r_0 and κ. With the increase of r_0 or κ, $V(r,\varphi)$ becomes a shallower potential.

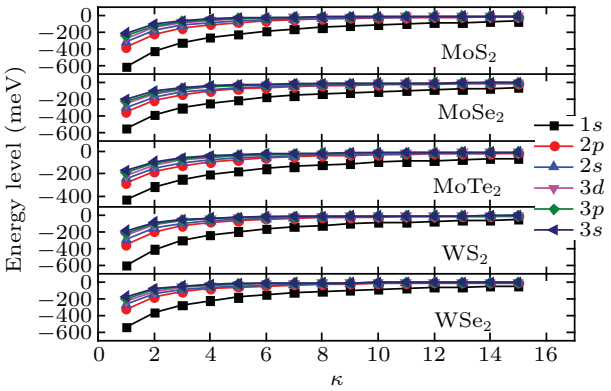


Fig. 2. Curves of energy level versus κ of hydrogenic donor impurity for six low-lying states of five ML TMDs.

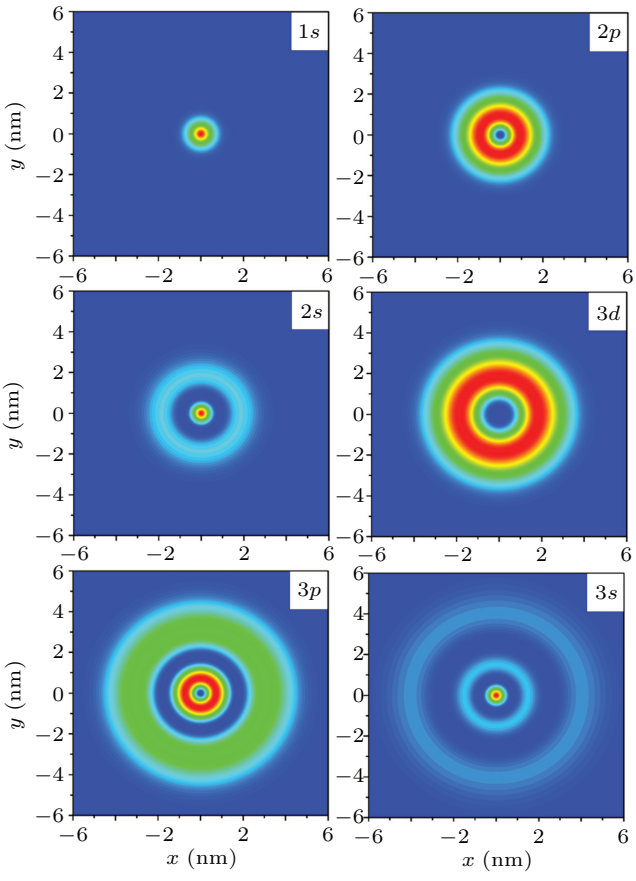


Fig. 3. Color map in plane *xy* representing amplitude of probability density for six low-lying impurity states as a function of *x* and *y* in ML MoS_2 with $\kappa = 1$, with density increasing from blue to red color.

In order to further understand the effect of electron spatial distribution on impurity states, we plot the color map that represents the calculated probability densities as a function of x and y for six low-lying impurity-bound electron states in an ML MoS_2 with $\kappa = 1$ in Fig. 3. The MoS_2 is taken as a representative member of TMDs. Here, the origin is in the center of the panel, x and y axes are oriented horizontally and vertically, respectively. As expected, these figures show that the probability densities are azimuthally symmetric with respect to the origin for all bound states. This is because the screened Coulomb potential has azimuthal symmetry. Only the probability density of the $1s$ state is almost concentrated in the origin. This indicates the wave function of 1s state is more localized around the impurity ion. On the other hand, the probability densities of $2p$, $3d$, and $3p$ state shown in the figure correspond to degenerate states. It should be noted that as n and $|l|$ increase, the probability density tends to spread out to larger values of r, and its magnitude is reduced. This means that it is farther from the impurity ion. The number of nodes (zeroes) in the open interval $(0,\infty)$ is $n-|l|-1$ in the radial wave function. For $l = 0$, the number of nodes increases incrementally from 0 to 2, going from $n = 1$ to $n = 3$.

3.2. Intersubband optical absorption spectra

In Fig. 4, we have illustrated the intersubband absorption spectra $\alpha(\hbar\omega)$ of a linear polarized light along the x direction as a function of photon energy $\hbar\omega$. The hydrogen donor impurity supplies one electron to the conduction band, so the intersubband optical transitions of donor states take place between conduction band states. In the ML TMD, the strong spin–orbit coupling leads to the large spin–orbit splitting of the valence band. Therefore, unlike exciton states in ML TMDs, the intersubband transitions of donor states do not have A nor B distinct type. Based on Eq. (8), one can conclude that the absorption coefficient is proportional to the intersubband oscillator strength. The peak value of absorption spectrum corresponds to the threshold photon energy, *i.e.*, $\hbar\omega \cong E_f - E_i$. In the absorption spectra, three sharp intersubband absorption peaks are clearly seen, which are dominated by the strong attractive Coulomb interaction between electron and donor ion as well as the impurity level degeneracy and the valley degeneracy. Of three intersubband transitions, the absorption peak of the $1s \to 2p$ transition is the strongest, while that of the $1s \to 4p$ transition is the weakest. Therefore, the main intersubband optical transition is considered to take place between the $1s$ and $2p$ states. This provides an opportunity for direct insight into the strong light–matter interaction in a 2D regime. The absorption peak position is known to correspond to the intersubband transition energy. For five TMDs, the relative ordering of their intersubband transition energy is found to be as follows: $MoTe_2 < MoSe_2 < WSe_2 < MoS_2 < WS_2$. This is because donor related optical transitions are related to the dielectric screening length and effective mass of electron. For MoS_2, the wavelengths corresponding to the resonance peaks are 5.25 μm, 3.30 μm, and 2.78 μm for $1s \to 2p$, $1s \to 3p$, and $1s \to 4p$ transitions, respectively. These wavelength ranges correspond to the so-called "mid-infrared region". The phonon absorption is the major obstacle to producing efficient light absorption based on intersubband transitions. Since an intersubband transition energy is much larger than an optical phonon energy, this very rapid nonradiative relaxation path would be effectively eliminated. In an ML MoS_2, the intensity ratio of $1s \to 2p$, $1s \to 3p$, and $1s \to 4p$ peaks is 1:0.091:0.027, while it is 1:0.181: 0.063 in a bare 2D hydrogen-like Coulomb potential, exhibiting the transitions of non-hydrogenic Rydberg series. Specifically, the confinement of electron together with the strongly reduced dielectric screening within a monolayer space results in the strong interaction of the electron with light, which can be utilized to fabricate highly sensitive mid-infrared photodetectors based on ML TMDs.

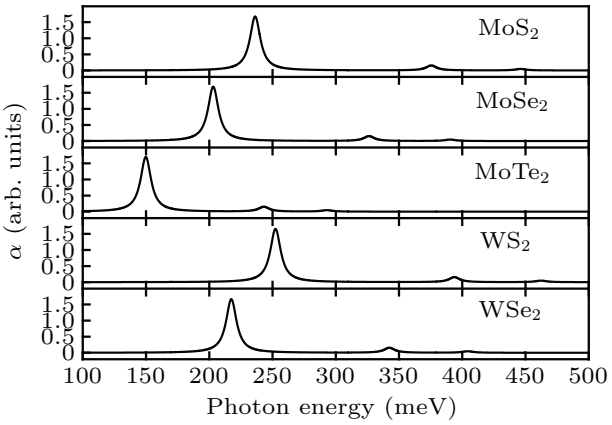


Fig. 4. Intersubband absorption spectra $\alpha(\hbar\omega)$ *versus* photon energy of linearly polarized light along x direction for five ML TMDs at $\kappa = 1$.

Figure 5 shows the plots of intersubband oscillator strength and transition energy versus κ of $1s \to 2p$, $1s \to 3p$, and $1s \to 4p$ transitions at linearly polarized light along the x direction for five ML TMDs. The variation trends of the intersubband oscillator strength and transition energy as a function of κ are similar to those for five TMDs. As κ increases, the intersubband oscillator strength of $1s \to 2p$ transition decreases monotonically. However, the intersubband oscillator strength of $1s \to 3p$ transition remains nearly constant and that of $1s \to 4p$ transition increases slightly. With κ increasing, the intersubband transition energy decreases monotonically. This is because the screening of Coulomb interaction by the dielectric environments weakens the binding of the electron by the

donor ion. For MoS_2, when κ increases from 1 to 15, the wavelength corresponding to the resonance peak ranges from 5.25 μm to 23.46 μm for $1s \rightarrow 2p$ transition. It means that the wavelength shifts to longer wavelengths, thus covering the mid-infrared window more completely.

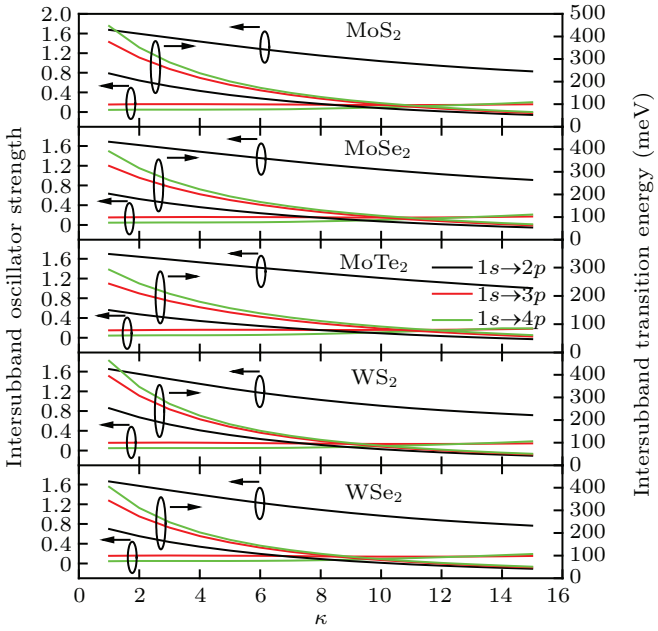


Fig. 5. Plots of intersubband oscillator strength and intersubband transition energy *versus* κ of $1s \rightarrow 2p$, $1s \rightarrow 3p$, and $1s \rightarrow 4p$ transitions under linearly polarized light along the x direction for five ML TMDs.

4. Conclusions

The hydrogenic donor impurity states and intersubband absorption spectra of ML MoS_2, $MoSe_2$, $MoTe_2$, WS_2, and WSe_2 under dielectric environments within the EMA are studied systematically in this work. A variationally optimized diagonalization method based on a 2D nonorthogonal associated Laguerre basis set is successfully applied to the ML TMDs. The results show that the 2D quantum confinement effect together with the strongly reduced dielectric screening results in the strong attractive Coulomb potential between electron and donor ion, with an exceptionally large impurity binding energy and a huge intersubband oscillator strength. Moreover, the impurity level degeneracy and the valley degeneracy increase the intersubband oscillator strength by four times. These lead to strong interaction of the electron with light in a 2D regime. The impurity electron series appears in an anomalous energy-level ordering of the orbital angular momentum caused by the dielectric screening effect. The intersubband absorption spectra of the ML TMDs exhibit strong absorption lines of the non-hydrogenic Rydberg series and depend strongly on the dielectric screening length. The strength of the Coulomb potential can be controlled by changing the dielectric environment. The electron affinity difference leads to charge transfer between ML TMD and the surrounding dielectric environment, generating the polarization-electric field in ML TMD accompanied by weakening the Coulomb interaction strength. The larger the dielectric constant of the dielectric environment, the more the charge transfer is, accompanied by the larger polarization-electric field with the stronger dielectric screening. The calculated results in this work are very useful in designing the next generation of mid-infrared photodetectors based on ML TMDs with dielectric environments.

Appendix A: Derivation of matrix elements of screened Coulomb potential

In this appendix, the analytical expression for the matrix element $V_{n'l',nl}$ of the screened Coulomb potential is derived.

The associated Laguerre polynomials are given explicitly by the formula

$$\mathrm{L}_n^{2|l|}(\zeta r) = \sum_{j=0}^{n} (-1)^j \binom{n+2|l|}{n-j} \cdot \frac{(\zeta r)^j}{j!}, \tag{A1}$$

where $\binom{n}{k}$ is a binomial coefficient. Substituting Eq. (A1) into Eq. (5b), the analytical representation of the radial wave function becomes

$$\begin{aligned} R_{nl}(r) = &\left[\frac{n!}{(n+2|l|)!(2n+2|l|+1)}\right]^{1/2} \zeta \\ &\times \exp\left(-\frac{\zeta r}{2}\right) \sum_{j=0}^{n} (-1)^j \binom{n+2|l|}{n-j} \\ &\times \frac{(\zeta r)^{j+|l|}}{j!}. \end{aligned} \tag{A2}$$

Owing to no explicit integrals involved in $V_{n'l',nl}$ of Eq. (7a), the integral identities are obtained as follows:[50]

$$\begin{aligned} &\int_0^\infty \mathrm{e}^{-ax} \mathrm{H}_\nu(bx) x^\lambda \,\mathrm{d}x \\ &= \frac{b^{\nu+1}\Gamma(\lambda+\nu+2)}{2^\nu a^{\lambda+\nu+2}\sqrt{\pi}\Gamma(\nu+3/2)} \\ &\quad \times {}_3\mathrm{F}_2\left(1, \frac{\lambda+\nu}{2}+1, \frac{\lambda+\nu+3}{2}; \frac{3}{2}, \nu+\frac{3}{2}; -\frac{b^2}{a^2}\right), \end{aligned} \tag{A3}$$

$$\begin{aligned} &\int_0^\infty \mathrm{e}^{-\alpha x} Y_\nu(\beta x) x^{\mu-1} \,\mathrm{d}x \\ &= -\frac{2}{\pi}\Gamma(\nu+\mu)(\beta^2+\alpha^2)^{-\mu/2} \mathrm{Q}_{\mu-1}^{-\nu}[\alpha(\alpha^2+\beta^2)^{-1/2}], \end{aligned} \tag{A4}$$

where ${}_3\mathrm{F}_2(a_1, a_2, a_3; b_1, b_2; x)$ is the generalized hypergeometric function with three parameters of type 1, and two parameters of type 2, $\mathrm{Q}_n^m(z)$ is the associated Legendre function of the second kind, and $\Gamma(x)$ is the Gamma function.

Then the matrix elements $V_{n'l',nl}$ become

$$
\begin{aligned}
V_{n'l',nl} &= \int_0^{2\pi}\int_0^{\infty} \Phi^*_{n'l'}(r)V(r,\varphi)\Phi_{nl}(r)r\mathrm{d}r\mathrm{d}\varphi \\
&= \delta_{l',l}\left(-\frac{e^2}{4\pi\kappa\varepsilon_0}\cdot\frac{\pi}{2r_0}\right)\left[\frac{n'!}{(n'+2|l'|)!(2n'+2|l'|+1)}\right]^{1/2}\left[\frac{n!}{(n+2|l|)!(2n+2|l|+1)}\right]^{1/2} \\
&\quad\times\sum_{j'=0}^{n'}\sum_{j=0}^{n}\zeta^{j'+|l'|+j+|l|+2}\frac{(-1)^{j'+j}}{j'!j!}\binom{n'+2|l'|}{n'-j'}\binom{n+2|l|}{n-j}\cdot\int_0^{\infty}\exp(-\zeta r)\left[\mathrm{H}_0\left(\frac{r}{r_0}\right)-\mathrm{Y}_0\left(\frac{r}{r_0}\right)\right]r^{j'+|l'|+j+|l|+1}\mathrm{d}r \\
&= \delta_{l',l}\left(-\frac{e^2}{4\pi\kappa\varepsilon_0}\cdot\frac{\pi}{2r_0}\right)\left[\frac{n'!}{(n'+2|l'|)!(2n'+2|l'|+1)}\right]^{1/2}\left[\frac{n!}{(n+2|l|)!(2n+2|l|+1)}\right]^{1/2} \\
&\quad\times\sum_{j'=0}^{n'}\sum_{j=0}^{n}\frac{(-1)^{j'+j}}{j'!j!}\binom{n'+2|l'|}{n'-j'}\binom{n+2|l|}{n-j}\left[\frac{\Gamma(j'+|l'|+j+|l|+3)}{\sqrt{\pi}\Gamma(\frac{3}{2})\zeta r_0}\right. \\
&\quad\times{}_3\mathrm{F}_2\left(1,\frac{j'+|l'|+j+|l|+3}{2},\frac{j'+|l'|+j+|l|+4}{2};\frac{3}{2},\frac{3}{2};-\frac{1}{\zeta^2r_0^2}\right) \\
&\quad\left.+\frac{2}{\pi}\Gamma(j'+|l'|+j+|l|+2)\zeta^{j'+|l'|+j+|l|+2}\left(\zeta^2+\frac{1}{r_0^2}\right)^{-(1/2)(j'+|l'|+j+|l|+2)}\mathrm{Q}^0_{j'+|l'|+j+|l|+1}\left(\frac{\zeta}{\sqrt{\zeta^2+1/r_0^2}}\right)\right]. \qquad \text{(A5)}
\end{aligned}
$$

References

[1] Borghardt S, Tu J S, Winkler F, Schubert J, Zander W, Leosson K and Kardynał B E 2017 *Phys. Rev. Materials* **1** 054001
[2] Tuan D V, Yang M and Dery H 2018 *Phys. Rev. B* **98** 125308
[3] Pang Y D, Wu E X, Xu Z H, Hu X D, Wu S, Xu L Y and Liu J 2021 *Chin. Phys. B* **30** 068501
[4] Ma J J, Wu K, Wang Z Y, Ma R S, Bao L H, Dai Q, Ren J D and Gao H J 2022 *Chin. Phys. B* **31** 088105
[5] Bian C, Shi J, Liu X, Yang Y, Yang H and Gao H 2022 *Chin. Phys. B* **31** 097304
[6] Wu J M, Li L H, Zheng W H, Zheng B Y, Xu Z Y, Zhang X H, Zhu C G, Wu K, Zhang C, Jiang Y, Zhu X L and Zhuang X J 2022 *Chin. Phys. B* **31** 057803
[7] Henriques J C G, Kamban H C, Pedersen T G and Peres N M R 2021 *Phys. Rev. B* **103** 235412
[8] Kusch P, Mueller N S, Hartmann M T and Reich S 2021 *Phys. Rev. B* **103** 235409
[9] Stepanov P, Vashisht A, Klaas M, Lundt N, Tongay S, Blei M, Höfling S, Volz T, Minguzzi A, Renard J, Schneider C and Richard M 2021 *Phys. Rev. Lett.* **126** 167401
[10] Mak K F, Lee C, Hone J, Shan J and Heinz T F 2010 *Phys. Rev. Lett.* **105** 136805
[11] Splendiani A, Sun L, Zhang Y, Li T, Kim J, Chim C Y, Galli G and Wang F 2010 *Nano Lett.* **10** 1271
[12] Mak K F, He K, Shan J and Heinz T F 2012 *Nat. Nanotechnol.* **7** 494
[13] Zeng H, Dai J, Yao W, Xiao D and Cui X 2012 *Nat. Nanotechnol.* **7** 490
[14] Cao T, Wang G, Han W, Ye H, Zhu C, Shi J, Niu Q, Tan P, Wang E, Liu B and Feng J 2012 *Nat. Commun.* **3** 887
[15] Chernikov A, Berkelbach T C, Hill H M, Rigosi A, Li Y, Aslan O B, Reichman D R, Hybertsen M S and Heinz T F 2014 *Phys. Rev. Lett.* **113** 076802
[16] Bastard G 1981 *Phys. Rev. B* **24** 4714
[17] Yen S T 2002 *Phys. Rev. B* **66** 075340
[18] Yen S T 2003 *Phys. Rev. B* **68** 165331
[19] ahin M 2008 *Phys. Rev. B* **77** 045317
[20] Perraud S, Kanisawa K, Wang Z Z and Fujisawa T 2008 *Phys. Rev. Lett.* **100** 056806
[21] Lin C Y and Ho Y K 2011 *Phys. Rev. A* **84** 023407
[22] Skinner B 2019 *Phys. Rev. Materials* **3** 104601
[23] Aghajanian M, Schuler B, Cochrane K A, Lee J H, Kastl C, Neaton J B, Weber-Bargioni A, Mostofi A A and Lischner J 2020 *Phys. Rev. B* **101** 081201
[24] Yang X C and Xing Y 2020 *Chin. Phys. B* **29** 087802
[25] W Chao, Li N, Dai N, Shi W Z, Hu G J and Zhu H 2021 *Chin. Phys. B* **30** 050702
[26] Wu W and Fisher A J 2021 *Phys. Rev. B* **104** 035433
[27] Pereira V M, Nilsson J and Neto A H C 2007 *Phys. Rev. Lett.* **99** 166802
[28] Noh J Y, Kim H, Park M and Kim Y S 2015 *Phys. Rev. B* **92** 115431
[29] Villari L D M, Galbraith I and Biancalana F 2018 *Phys. Rev. B* **98** 205402
[30] Wang G, Chernikov A, Glazov M M, Heinz T F, Marie X, Amand T and Urbaszek B 2018 *Rev. Mod. Phys.* **90** 021001
[31] Tuan D V, Yang M and Dery H 2018 *Phys. Rev. B* **98** 125308
[32] Prazdnichnykh A I, Glazov M M, Ren L, Robert C, Urbaszek B and Marie X 2021 *Phys. Rev. B* **103** 085302
[33] Yang X C, Yu H and Wang Y 2021 *Phys. Rev. B* **104** 245305
[34] Perdew J P, Burke K and Ernzerhof M 1996 *Phys. Rev. Lett.* **77** 3865
[35] Hashemi A, Krasheninnikov A V, Puska M and Komsa H P 2019 *Phys. Rev. Materials* **3** 023806
[36] Anvari R, Zaremba E and Dignam M M 2021 *Phys. Rev. B* **104** 155402
[37] Kohn W and Luttinger J M 1955 *Phys. Rev.* **97** 883
[38] Kohn W and Luttinger J M 1955 *Phys. Rev.* **98** 915
[39] Wu S, Cheng L and Wang Q 2017 *Mater. Res. Express* **4** 085017
[40] Li S S 1993 *Semiconductor Physical Electronics* (Boston: Springer US) p. 246
[41] Lax M 1960 *Phys. Rev.* **119** 1502
[42] Orlova E E and Harrison P 2004 *Appl. Phys. Lett.* **85** 5257
[43] Keldysh L V 1979 *JETP Lett.* **29** 658
[44] Cudazzo P, Tokatly I V and Rubio A 2011 *Phys. Rev. B* **84** 085406
[45] Berkelbach T C, Hybertsen M S and Reichman D R 2013 *Phys. Rev. B* **88** 045318
[46] Wu S, Cheng L and Wang Q 2019 *Phys. Rev. B* **100** 115430
[47] Wu S 2022 *Physica E* **141** 115238
[48] Luttinger J M 1956 *Phys. Rev.* **102** 1030
[49] Robertson J 2004 *Eur. Phys. J.: Appl. Phys.* **28** 265
[50] Gradshteyn I S and Ryzhik I M 2007 *Table of Integrals, Series, and Products*, 7th edn. (Amsterdam: Academic) pp. 700–755